Journal of Materials Science: Materials in Electronics (2020) 31:2022–2029
https://doi.org/10.1007/s10854-019-02721-y

Synthesis of tubular g-C_3N_4 via a H_2SO_4-assisted precursor self-assembly strategy for enhanced photocatalytic degradation of organic pollutant

Minfeng Cao[1] · Jianliang Zuo[1] · Yongchao Huang[1,2] · Zili Liu[1]

Received: 14 September 2019 / Accepted: 8 December 2019 / Published online: 16 December 2019

Abstract
Nanostructured graphitic carbon nitride (g-C_3N_4) has attracted enormous attention as a promising visible-light photocatalyst because of its unique physicochemical properties. However, controlling the nanostructure of g-C_3N_4 is challenging because the most common template methods are high-cost and high-risk intensive as well as tedious. In this work, tubular g-C_3N_4 is prepared in situ by annealing a melamine-cyanurate supramolecular array, which is conducted through a H_2SO_4-assisted precursor self-assembly strategy. The as-prepared samples are characterized by X-ray diffraction, scanning electron microscopy, Brunauer–Emmett–Teller analysis, and other photoelectrochemical measurements. Moreover, the band structure of the g-C_3N_4 nanotubes is investigated to elucidate the carrier separation mechanism. The result shows that the g-C_3N_4 nanotubes have a hollow structure (average diameter: 0.2–1.2 μm, length: 10–50 μm, and thickness: 15–20 nm) and an enhanced electronic structure. Owing to the high specific surface area of their hierarchical pores and the efficient charge separation of their 1D feature, the g-C_3N_4 nanotubes exhibit high photocatalytic methylene blue (MB)/tetracycline (TC) degradation rates of 0.0265 min^{-1} and 0.0110 min^{-1}, which are three and seven times higher than those of Bulk g-C_3N_4, respectively. Therefore, this study provides a facile and effective strategy for the construction of carbon nitride nanostructures.

1 Introduction

Solar-driven photocatalysis has become one of the most effective methods to solve environmental and energy problems [1–4]. An effective photocatalyst for this reaction requires a strong oxidative ability, suitable band gap, and excellent stability in water solutions. In recent years, graphitic carbon nitride (g-C_3N_4) has become a prominent photocatalyst because of its non-toxicity, stability, simple preparation, and suitable band gap [5–7]. However, g-C_3N_4 possesses several disadvantages, including low specific surface area, high recombination rate, low transmission rate of charge carriers, and insufficient quantum efficiency, thus limiting its practical applications [8–13]. Meanwhile, considerable effort has been devoted to resolving these drawbacks through methods, such as morphology modification (exfoliation, nanostructure construction), doping (metal/non-metal element), composite (heterojunction construction), etc. [14–17]. Among these methods, supramolecular preassembly is a promising strategy that can produce g-C_3N_4 with an ordered texture and a controllable morphology [18]. For example, Huang et al. [19] prepared various g-C_3N_4 structures including 3D architectures, 2D ultra-thin nanosheets, and 1D arrays through thermal treatment of the melamine-cyanuric acid supramolecular. The unique electronic structure of different topographies facilitates an astonishing photocatalytic performance. This interesting preparation strategy justifies further exploration.

In particular, the construction of g-C_3N_4 nanotubes is considered to be one of the most effective methods to improve its photocatalytic activity. The anisotropic growth

Electronic supplementary material The online version of this article (https://doi.org/10.1007/s10854-019-02721-y) contains supplementary material, which is available to authorized users.

✉ Yongchao Huang
huangych@gzhu.edu.cn

✉ Zili Liu
gzdxlzl@163.com

[1] School of Chemistry and Chemical Engineering, Guangzhou University, Guangzhou 510006, China

[2] Institute of Environmental Research at Greater Bay Area, Key Laboratory for Water Quality and Conservation of the Pearl River Delta, Ministry of Education, Guangzhou Key Laboratory for Clean Energy and Materials, Guangzhou University, Guangzhou 510006, China

of 1D structure is conducive to the transmission of photogenerated electrons [20–23], and the hollow structure is expected to enhance the multiple scattering effect of visible light in the tube [24]. However, the synthesis of tubular carbon nitride often involves hazardous reagents and expensive templates, leading to tedious post-treatment problems [12, 25, 26]. Cao et al. [27] fabricated tubular g-C_3N_4 via a chemical method, and the as-prepared g-C_3N_4 showed a high specific capacitance and good photodegradation ability. However, it should be pointed out that a large amount of HNO_3 was used as solvent, which necessitates further exploration and enhancement. Consequently, the development of a facile, green, and efficient method to prepare tubular carbon nitride is required.

Herein, we developed a H_2SO_4-assisted precursor self-assembly strategy to prepare carbon nitride nanotubes. Particularly, melamine-cyanurate supramolecular array (SMCA) was first formed via a H_2SO_4-assisted hydrothermal treatment and further polymerized to form carbon nitride nanotubes by the subsequent annealing. Different from the high consumption of H_2SO_4 in chemical exfoliation [28] of g-C_3N_4, a spot of H_2SO_4 here was serving as a revulsive, leading an interesting change of morphology and electronic structure of the as-prepared g-C_3N_4. Because of the hierarchical pores and 1D feature, g-C_3N_4 nanotubes exhibit a large specific surface area and excellent charge separation, and thus show good photocatalytic degradation performance.

2 Experimental

2.1 Synthesis of H_2SO_4-modified melamine-cyanurate (SMCA) precursors

Typically, 4.0 g melamine was dispersed into 30 mL of deionized water. Certain amount of H_2SO_4 (0 mL, 1 mL, 1.5 mL, 2 mL, 2.5 mL) was added to the solution after which the resulting suspension was stirred for 30 min at ambient temperature. The white viscous suspension was then transferred to a 100-mL Teflon-lined autoclave and heated at 180 °C for 12 h, respectively. After cooling to ambient temperature, the obtained supramolecular aggregates (labeled as SMCA-0, SMCA-1, SMCA1.5, SMCA-2, and SMCA-2.5) were collected by washing with deionized water and ethanol. Finally, the SMCA were dried at 80 °C.

2.2 Synthesis of tubular g-C_3N_4

A series of tubular g-C_3N_4 were successfully prepared by direct calcination of the as-made *S*MCA precursors. The SMCA precursors were placed into a 50-mL corundum crucible with a cover, heated in a muffle furnace at a rate of 5 °C/min, and kept for 3 h at 500 °C to obtain the yellow g-C_3N_4 products (labeled as SCN-0, SCN-1, SCN-1.5, SCN-2). There was no product when annealing SMCA-2.5. Bulk g-C_3N_4 (BCN) was synthesized by directly heating the melamine at 550 °C for 3 h.

Characterization and photocatalytic tests are described in Supplementary Information.

3 Results and discussion

The morphologies of the precursors are investigated via scanning electron microscopy (SEM) analysis. As shown in Fig. 1a, SMCA-2 shows a dense rod-like array with a smooth and regular surface, which is completely different from the monoclinic pristine melamine particles (Fig. S1a). H_2SO_4-assisted hydrothermal treatment has a great impact on the morphology of SMCA (further discussed in the supplementary document). The high-magnification SEM images further depict the morphologies of samples. As shown in Fig. 1, SCN-1(Fig. 1b) and SCN-1.5 (Fig. 1c) display a rod-like structure with carbon nitride nanosheets stacking inside, and the stacking nanosheets delaminate from inside and begin to separate from the tube wall. Typically, SCN-2 (Fig. 1d) maintains a tubular structure with a diameter in the range of 0.2–1.2 μm and a length of 10–50 μm. Moreover, several pores with a diameter of 10–20 nm are observed on the tube wall of SCN-2, which would offer a large surface area for accommodating reaction substrate. In comparison, BCN (Fig. S2a) and SCN-0 (Fig. S2b) present a classical bulk structure with severe agglomeration and smooth, imporous surfaces. No product is obtained when annealing SMCA-2.5, which suggests that melamine will hydrolyze in high doses of H_2SO_4.

Transmission electron microscopy (TEM) image (Fig. 1e) shows that SCN-2 has a nanotube structure with a diameter of hundreds of nanometers and a wall thickness in the range of 15–20 nm, which is consistent with the SEM image. The N_2 adsorption–desorption isotherm (Fig. 1f) shows that the BET surface area of SCN-2 is 92.04 m^2/g, which is 5.7 times more than BCN (16.26 m^2/g). BJH (inset in Fig. 1f) analysis indicates that SCN-2 has hierarchical pores distributed on a range of 2–4 nm and 38–52 nm, which may correspond to the mesopores on the nanotubes and the interstices between the nanotubes, respectively. The hollow structure and hierarchical porous feature of SCN improve its active specific surface area, and are conducive for exposing more interfaces to come into contact with the reactant, thereby exhibiting superior adsorption and photocatalytic properties.

To elucidate the transformation of the precursor, the chemical structure is determined via X-ray diffraction (XRD). Typically, pristine melamine can be well indexed to monoclinic melamine (JCPDSNo: 39-1960), while the XRD pattern of SMCA is indexed to melamine cyanurate

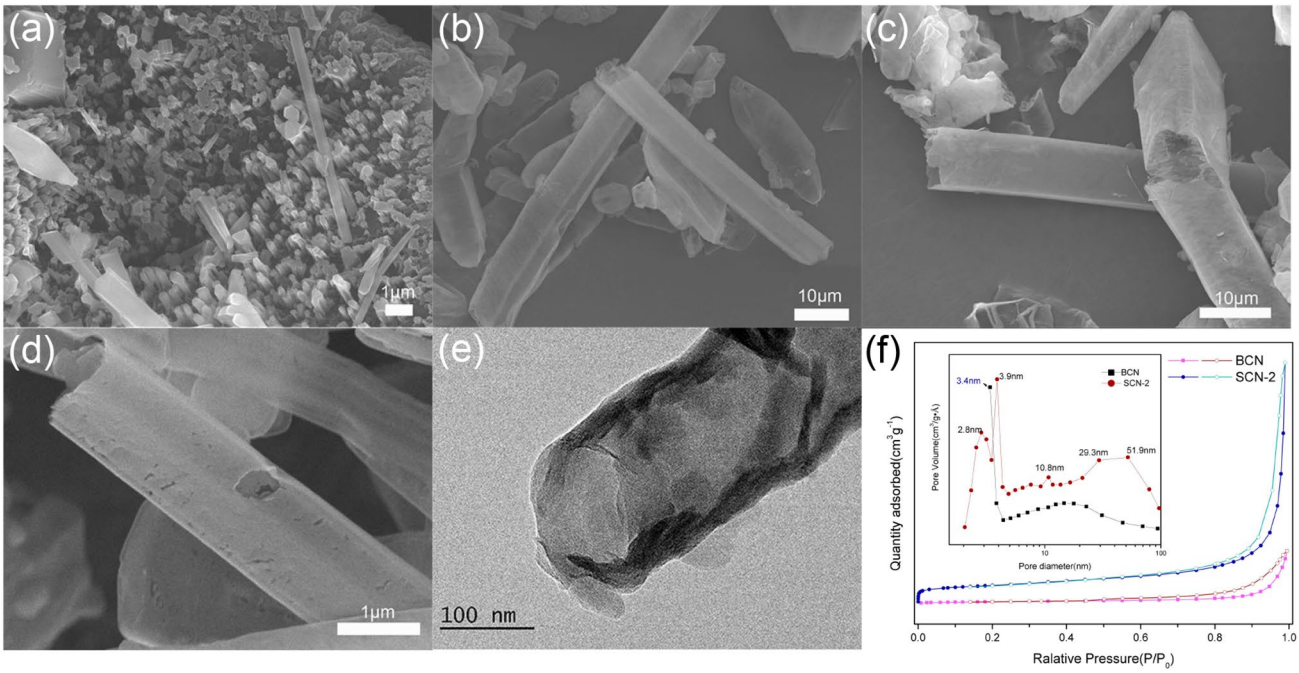

Fig. 1 SEM images of **a** SMCA-2, **b** SCN-1, **c** SCN-1.5, **d** SCN-2, **e** TEM images of SCN-2, **f** N_2 adsorption isotherms (Inset: pore size distribution) of SCN-2 and BCN

(JCPDSNo: 05-0127), suggesting the formation of a supramolecule (SMCA inset in Fig. 2a). Moreover, SMCA-2.5 shows a completely different XRD pattern from melamine and melamine cyanurate and it can be well indexed to cyanuric acid (JCPDS No: 23-1637), indicating that most of the melamine are converted to cyanuric acid with the H_2SO_4 amount reaching 2.5 mL and thus leading a precipitous drop in production. These results are consistent with SEM (Fig. S1).

The structure of the sample is also evaluated by XRD. Figure 2b reveals that SCN and BCN present two peaks at 12.8° and 27.7°, corresponding to the (100) and (002) planes of carbon nitride [29]. Two peaks of SCN-2 are weaker than BCN, indicating that the crystallinity and the agglomeration of SCN-2 have decreased [30]. This result may be because the tubular structure disrupts the in-plane repetition of the heptazine unit and weakens the stacking of aromatic structure. FTIR spectra in Fig. 2c illustrate that SCN-2 has characteristic peaks at 810 cm^{-1}, 1200–1700 cm^{-1}, and 3000–3300 cm^{-1}, corresponding to the vibrations of the tri-s-triazine unit, heterocycles, and N–H of carbon nitride, respectively [31]. Based on the results above, a possible formation mechanism is proposed. First, part of melamine turns into cyanuric acid and the rod-like supramolecular compounds formed by self-assembly between melamine and cyanuric acid during the hydrothermal treatment. Then, rod-like carbon nitride is obtained by annealing SMCA. Furthermore, with the assistance of H_2SO_4, the conversion of melamine is accelerated, and a greater amount of cyanuric acid decomposes during thermal treatment, which reduces agglomeration of carbon nitride, leading to the formation of nanotube.

From N1s spectra (Fig. 3a), SCN-2 shows four peaks at 398.32 eV, 399.03 eV, 400.62 eV, and 404.35 eV, corresponding to N atom of C–N=C, N–$(C)_3$, N–H_x, and π excitation [32]. The peaks of SCN-2 shift to lower binding energies compared with those of BCN, indicating the formation of N vacancies [33]. Furthermore, from Table S1, the ratio of sp^2 C–N=C bonds(N_{2C}) to the sum of N–$(C)_3$ and N–H_x bonds is 0.91, which is lower than that of BCN (2.43), suggesting the preferential loss of N_{2C} atoms according to the calculation results [34]. To further confirm the existence of N vacancies, EPR is conducted to detect the spin state of unpaired electrons. In Fig. 3b, SCN-2 and CN show a single Lorentzian line with a g-value of 2.003, which can be due to lone paired electrons of sp^2-C in heptazine g-C_3N_4 [33]. Furthermore, SCN-2 shows a stronger EPR intensity than that of BCN, indicating the enriched N_{2C} defect on SCN-2 surface. For g-C_3N_4, intrinsic point defects would serve as recombination centers, while surface defects are conducive to boost charge separation [35]. Therefore, the N_{2C} defect on the SCN-2 surface may trap a portion of electrons, and thus quench the recombination of charge carriers [33, 36]. In addition, Raman spectra were carried out to better understand the chemical structure of SCN-2. As shown in Fig. S3, the main peaks at 705 and 974 cm^{-1} are attributed to

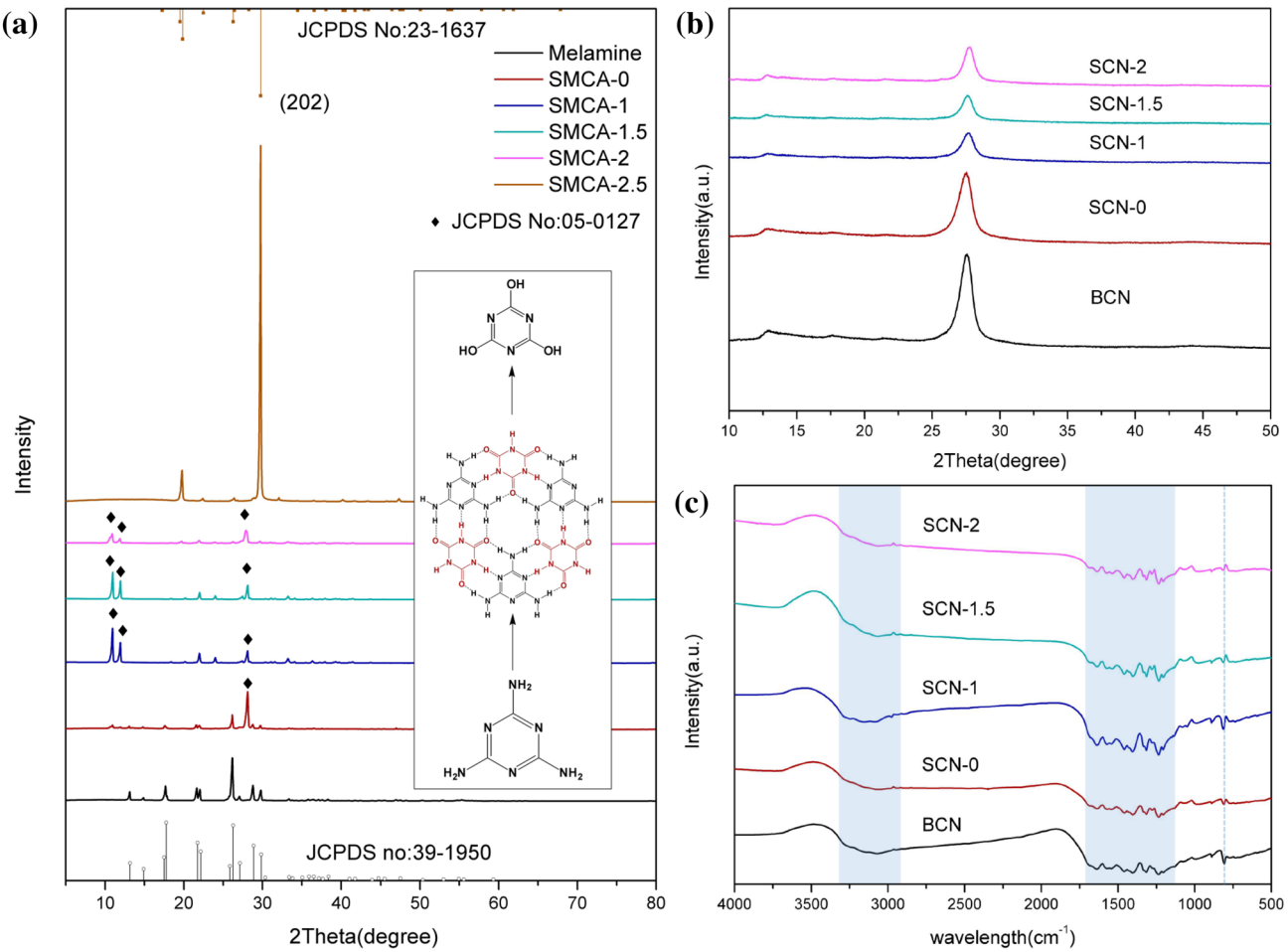

Fig. 2 XRD patterns of **a** melamine and SMCAs, **b** BCN and SCN, **c** FTIR spectra of BCN and SCN

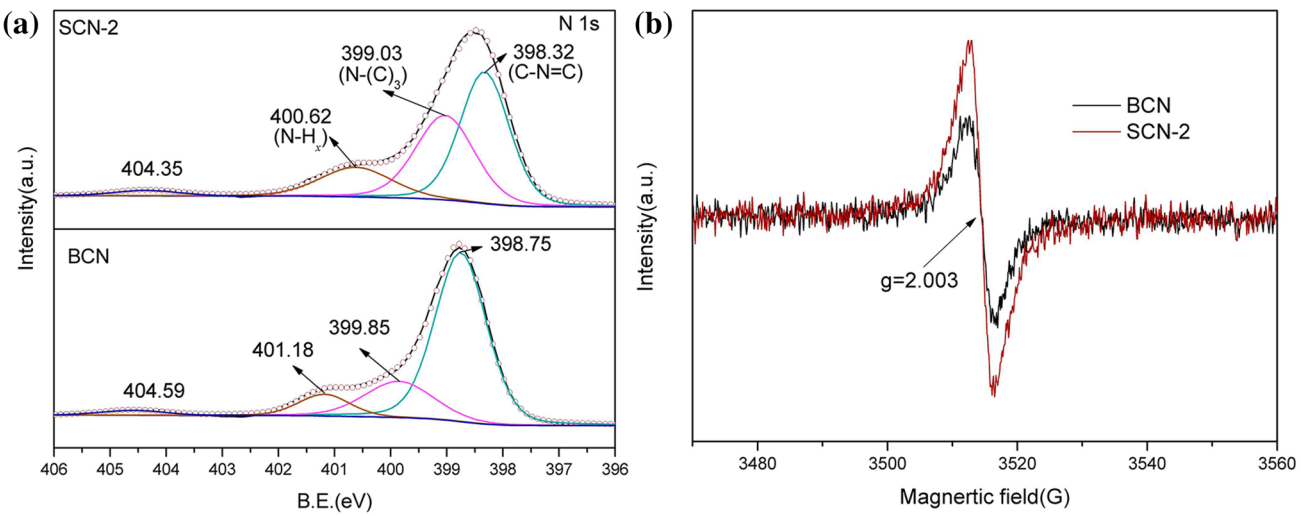

Fig. 3 **a** High-resolution N1s XPS spectra, **b** EPR spectra of SCN-2 and BCN

symmetric N-breathing mode of heptazine units and the in-plane bending vibrations of the tri-heptazine CNC linkages [37]. In addition, the peak at 762 cm^{-1} for BCN corresponds to the out-of-plane bending mode of graphitic domains of g-C_3N_4 [38]. This peak shifts to 766 cm^{-1} for SCN-2, which may be attributed to presence of the N vacancies and the tubular structure of SCN.

In Fig. 4a, UV–vis DRS of SCN-2 shows a blue-shift compared to BCN, which may be due to the quantum confinement effect caused by nanostructure [39]. According to the Tauc plot (inset of Fig. 4a), the band gap energy (E_g) of SCN-2 and BCN is determined to be 2.78 eV and 2.55 eV. Changes in optical properties induced by nanostructures can be also found in the photoluminescence (PL) spectra (Fig. 4b). The main peak of SCN-2 shows a blue-shift at approximately 440 nm and its overall intensity is much lower than that of BCN. In addition, SCN-2 shows a smaller radius in electrochemical impedance spectra Nyquist plots (Fig. 4c), suggesting lower electron transfer resistance. These results indicate that the 1D structure of SCN-2 might promote the migration of photogenic carriers and thus suppress charge recombination.

Furthermore, the energy band structures including the band gap, conduction band (CB), and valence band (VB) are studied to better understand the carrier separation mechanism. From the VB-XPS spectra in Fig. 4c, the energy gap between VB and the Fermi level (E_f) of BCN and SCN-2 could be determined to be 2.26 eV and 1.89 eV, respectively. Based on the Mott–Schottky plots in Fig. 4d, the flat potentials of BCN and SCN-2 were calculated to be −0.66 V and −0.52 V versus the Ag/AgCl electrode, respectively, and they could be converted to −0.46 V and −0.32 V versus the normal hydrogen electrode (NHE). Generally, the value of flat potentials is approximately equal to that of the Fermi level [40, 41]. Therefore, the VB positions of BCN and SCN-2 are equal to 1.80 eV and 1.57 eV, respectively. Based on abovementioned band gap energy, the CB positions of BCN and SCN-2 are −0.76 eV and −1.21 eV, respectively. The illustration of the band structure of BCN and SCN-2 is present in Fig. 4f. According to the band structure, SCN-2 presents a wider band gap and a large offset of CB positions. Since the CB position of samples refers to reduction potential, while that of the VB refers to the oxidation potential, a large negative shift of CB and rather high position of VB of SCN-2 are helpful for the generation of active radicals, such as h^+ and $\cdot O_2^-$. With its unique electronic structure, SCN-2 is expected to deliver a superior photo-oxidation activity. Mott–Schottky measurement could also determine the carrier density on the formation of Schottky barrier between anode and electrolytes. Generally, the carrier density (N_D) can be estimated from the slope of Mott–Schottky curve through the Poisson Eqs. (1) and (2) [42, 43]

$$\frac{1}{C^2} = \frac{2}{e\varepsilon\varepsilon_0 N_D}\left(E - E_{fb} - \frac{\kappa T}{e}\right), \tag{1}$$

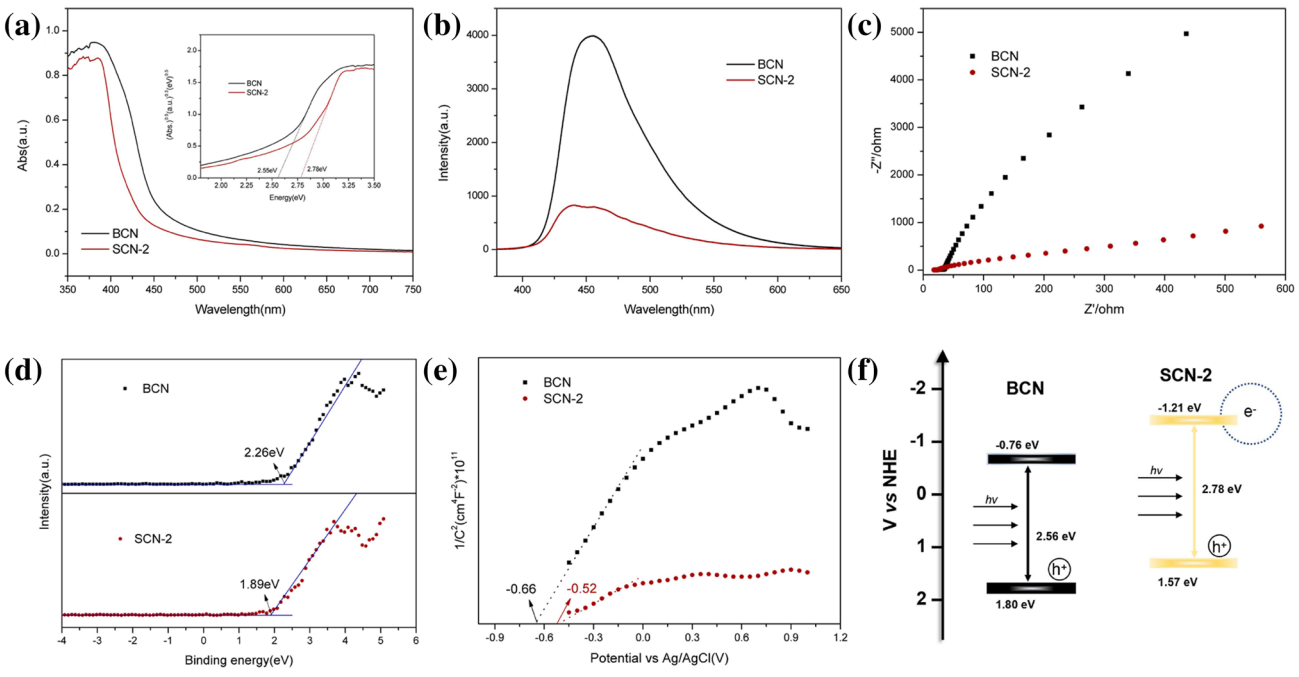

Fig. 4 **a** UV–vis absorption curves. (Inset: Tauc plots and band gaps), **b** PL spectra, **c** EIS spectra, **d** VB-XPS spectra, **e** Mott–Schottky plots, **f** band structure of BCN and SCN

$$N_D = \left(2/\varepsilon\varepsilon_0 e\right)\left[d\left(1/C^2\right)/dV\right]^{-1}, \quad (2)$$

where C denotes the capacitance of the space charge layer; ε denotes the dielectric constant; ε_0 denotes the vacuum permittivity (8.854×10^{-14} F/cm); e denotes the electron charge (1.602×10^{-19} C); E denotes the potential versus normal hydrogen electrode (NHE); κ denotes the Boltzmann constant (1.38×10^{-23} J/K). With the ε value of 15.6 for g-C_3N_4 [44], the N_D of SCN-2 is determined to be 9.4×10^{18}, which is 3 times higher than that of BCN (3.2×10^{18}). This result shows that the charge separation and transport efficiency are enhanced with tubular structure of SCN-2, which is consistent with the results of PL and EIS.

The photocatalytic performance of samples is evaluated through photodegradation of MB (20 mg/L) and TC (10 mg/L) in an aqueous solution under visible-light irradiation ($\lambda > 420$ nm). Photocatalytic degradation of MB (Fig. 5a, b) and TC (Fig. 5c, d) show that photocatalytic activity is significantly affected by the amount of H_2SO_4 used in the hydrothermal treatment. In view of its unique physicochemical properties, tubular SCN-2 shows superior activity both in the adsorption of dark conditions and degradation under illumination than that of BCN. After exposure to visible light for 60 min, the removal efficiency and reaction kinetic rate constant of MB reach 90 % and 0.0265 min^{-1}, respectively, which is 3 times higher than that of BCN (0.0084 min^{-1}), while the reaction kinetic rate constant of TC reaches 0.01101 min^{-1}, i.e., 7 times than that of BCN (0.00157 min^{-1}).

Active species capture experiments are performed in order to further clarify the photocatalytic mechanism and active species for MB degradation. In these experiments, ammonium oxalate (AO, 2 mmol), benzoquinone (BQ, 0.2 mmol), and isopropyl alcohol (IPA, 2 mmol) are used to scavenge holes (h^+), superoxide radical anions ($\cdot O_2^-$), and hydroxyl radicals (·OH), respectively. As shown in Fig. 6a, there is no significant change in the photocatalytic activity as the IPA is added, indicating the ·OH is not the main active oxidation species in MB degradation. In contrast,

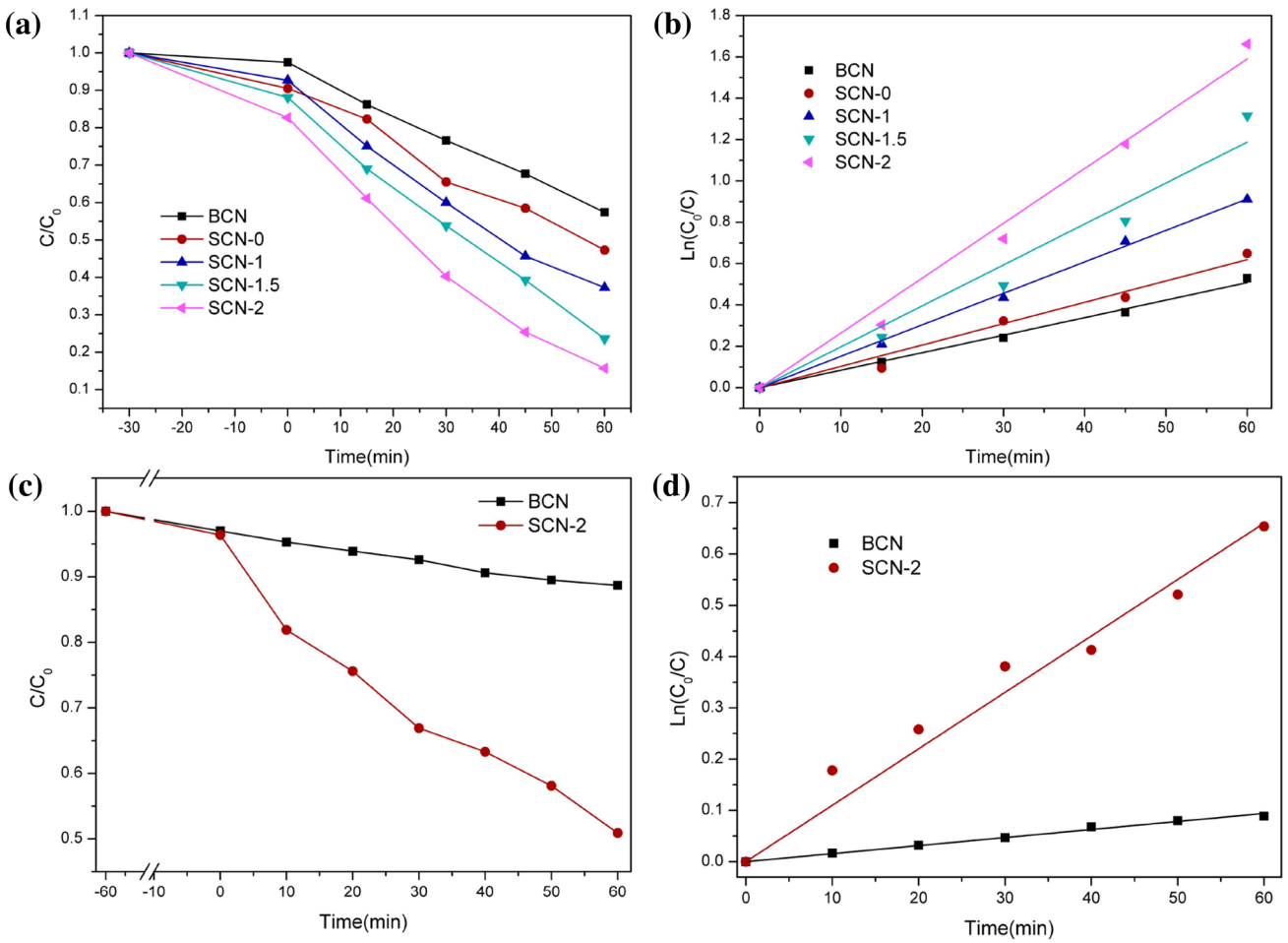

Fig. 5 MB (**a**, **b**), TC (**c**, **d**) degradation efficiency and kinetic linear simulation curves of BCN and SCN

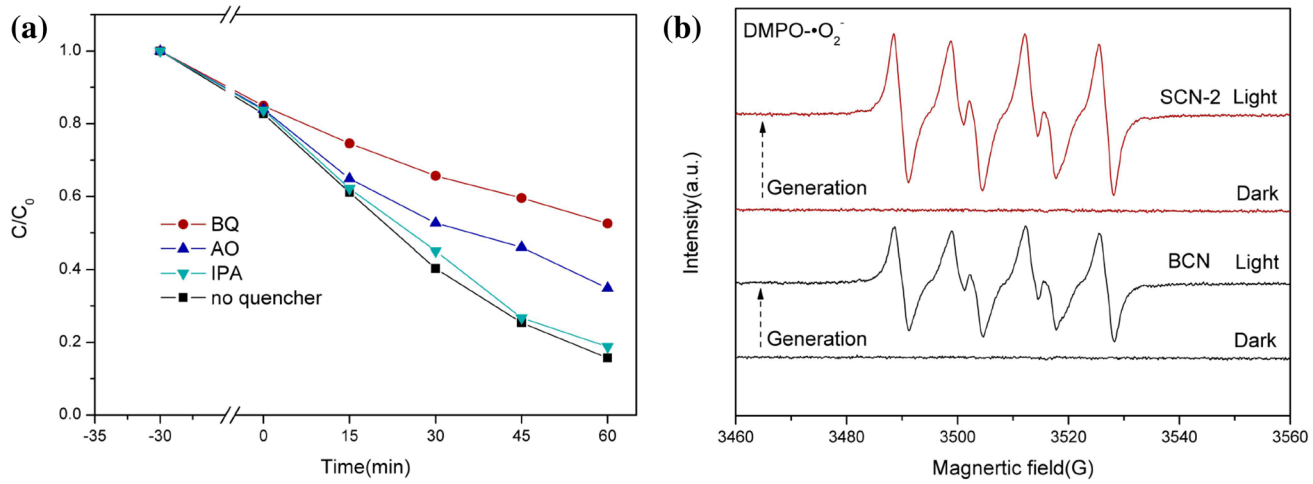

Fig. 6 **a** Trapping experiment, **b** EPR/DMPO-·O_2^- spectra of BCN and SCN-2

the photocatalytic activity is considerably suppressed by the introduction of BQ. According to the band structure, the VB potential of BCN (1.80 eV) and SCN-2 (1.57 eV) are not sufficiently higher enough than the standard redox potential of OH^-/·OH (1.99 eV vs NHE, pH = 7) [45]; thus, it is rational to infer that OH^- anion cannot be oxidized to ·OH by h^+. Notably, the CB potential of SCN-2 (− 1.21 eV) is much lower than that of BCN (− 0.76 eV), which is conducive for the generation of ·O_2^-. The EPR/DMPO experiment is also carried out for further analysis. In Fig. 6b, the peaks of DMPO-·O_2^- are obvious under illumination while no such signals are detected in dark condition, suggesting that dissolved oxygen can be transformed into ·O_2^- by photo-induced electron. Moreover, the intensity of the characteristic peak for SCN-2 is much stronger than that of BCN, which can be matched to the results of degradation experiments. This might attribute to the unique band structure and the rapid charge migration which can be featured by the 1D structure of SCN-2. Based on the abovementioned results, it is expected that ·O_2^- is the main active oxidation species for the degradation.

4 Conclusions

We fabricate g-C_3N_4 nanotubes by a simple H_2SO_4-assisted precursor self-assembly strategy. The results of XPS, DRS, and PL show that the N_{2C} defect, nanosize, and 1D structure might boost the transmission of the photogenerated carriers and further suppress charge recombination. The study of the band structures shows that SCN-2 had a wider band gap and a large offset of the CB positions which is expected to deliver a better photo-oxidation activity. Benefiting from the high specific surface area provided by the hierarchical pores and the hollow structure, SCN-2 shows excellent photocatalytic degradation of MB and TC, and the degradation rates reach 0.0265 min^{-1} and 0.0110 min^{-1}, respectively, which are 3 and 7 times higher than that of BCN. This study proposes a facile and effective method to prepare carbon nitride nanotubes and provides a feasible strategy for photocatalytic environmental remediation.

Acknowledgements This work was supported by the National Science Foundation of China (21676060 and 21706295), Guangzhou Research Collaborative Innovation Projects (201704020005), Foundation for Distinguished Young Talents in Higher Education of Guangdong (2016KQNCX123), and the Pearl River S&T Nova Program of Guangzhou (201906010024).

References

1. C.C. Wang, J.R. Li, X.L. Lv, Y.Q. Zhang, G.S. Guo, Energy Environ. Sci. **7**, 2831 (2014). https://doi.org/10.1039/c4ee01299b
2. Z. Tong, D. Yang, Z. Li et al., ACS Nano **11**, 1103 (2017). https://doi.org/10.1021/acsnano.6b08251
3. J.Q. Wen, J. Xie, Z.H. Yang et al., ACS Sustain. Chem. Eng. **5**, 2224 (2017). https://doi.org/10.1021/acssuschemeng.6b02490
4. Y.C. Huang, Z.J. Guo, H. Liu et al., Adv. Funct. Mater. **29**, 9 (2019). https://doi.org/10.1002/adfm.201903490
5. X. Wang, K. Maeda, A. Thomas et al., Nat. Mater. **8**, 76 (2009). https://doi.org/10.1038/nmat2317
6. Y.S. Jun, J. Park, S.U. Lee, A. Thomas, W.H. Hong, G.D. Stucky, Angew. Chem. Int. Ed. Engl. **52**, 11083 (2013). https://doi.org/10.1002/anie.201304034
7. Y.S. Jun, E.Z. Lee, X.C. Wang, W.H. Hong, G.D. Stucky, A. Thomas, Adv. Funct. Mater. **23**, 3661 (2013). https://doi.org/10.1002/adfm.201203732
8. S. Samanta, S. Martha, K. Parida, ChemCatChem **6**, 1453 (2014). https://doi.org/10.1002/cctc.201300949
9. J.F. Zhang, Y.F. Hu, X.L. Jiang, S.F. Chen, S.G. Meng, X.L. Fu, J. Hazard. Mater. **280**, 713 (2014). https://doi.org/10.1016/j.jhazmat.2014.08.055
10. H. Gao, H. Yang, J. Xu, S. Zhang, J. Li, Small. (2018). https://doi.org/10.1002/smll.201801353

11. J. Zhang, M. Wu, B.B. He, R. Wang, H.W. Wang, Y.S. Gong, Appl. Surf. Sci. **470**, 565 (2019). https://doi.org/10.1016/j.apsusc.2018.11.165
12. F. Kamali, M.M. Eskandari, A. Rashidi, M. Baghalha, M. Hassanisadi, T. Hamzehlouyan, J. Hazard. Mater. **364**, 218 (2019). https://doi.org/10.1016/j.jhazmat.2018.09.095
13. Z. Zhang, K. Liu, Z. Feng, Y. Bao, B. Dong, Sci Rep. **6**, 19221 (2016). https://doi.org/10.1038/srep19221
14. P. Kumar, R. Boukherroub, K. Shankar, J. Mater. Chem. A **6**, 12876 (2018). https://doi.org/10.1039/c8ta02061b
15. M.S. Nasir, G.R. Yang, I. Ayub et al., Appl. Catal. B **257**, 37 (2019). https://doi.org/10.1016/j.apcatb.2019.117855
16. Y.Y. Li, B.X. Zhou, H.W. Zhang et al., Nanoscale **11**, 6876 (2019). https://doi.org/10.1039/c9nr00229d
17. B. Li, Y. Si, B.X. Zhou et al., ACS Appl. Mater. Interfaces. **11**, 17341 (2019). https://doi.org/10.1021/acsami.8b22366
18. G.F. Liao, Y. Gong, L. Zhang, H.Y. Gao, G.J. Yang, B.Z. Fang, Energy Environ. Sci. **12**, 2080 (2019). https://doi.org/10.1039/c9ee00717b
19. B.X. Zhou, S.S. Ding, B.J. Zhang et al., Appl. Catal. B **254**, 321 (2019). https://doi.org/10.1016/j.apcatb.2019.05.015
20. G.G. Zhang, A. Savateev, Y.B. Zhao, L.N. Li, M. Antonietti, J. Mater. Chem. A **5**, 12723 (2017). https://doi.org/10.1039/c7ta03777e
21. J. Gao, Y. Zhou, Z. Li, S. Yan, N. Wang, Z. Zou, Nanoscale **4**, 3687 (2012). https://doi.org/10.1039/c2nr30777d
22. S. Guo, Z. Deng, M. Li et al., Angew. Chem. Int. Ed. Engl. **55**, 1830 (2016). https://doi.org/10.1002/anie.201508505
23. S.W. Zhang, L.P. Zhao, M.Y. Zeng, J.X. Li, J.Z. Xu, X.K. Wang, Catal. Today **224**, 114 (2014). https://doi.org/10.1016/j.cattod.2013.12.008
24. H. Li, X.Q. Yan, B. Lin et al., Nano Energy **47**, 481 (2018). https://doi.org/10.1016/j.nanoen.2018.03.026
25. M. Tahir, C.B. Cao, F.K. Butt et al., CrystEngComm **16**, 1825 (2014). https://doi.org/10.1039/c3ce42135j
26. S.W. Bian, Z. Ma, W.G. Song, J. Phys. Chem. C **113**, 8668 (2009). https://doi.org/10.1021/jp810630k
27. M. Tahir, C.B. Cao, F.K. Butt et al., J. Mater. Chem. A **1**, 13949 (2013). https://doi.org/10.1039/c3ta13291a
28. J. Xu, L.W. Zhang, R. Shi, Y.F. Zhu, J. Mater. Chem. A **1**, 14766 (2013). https://doi.org/10.1039/c3ta13188b
29. M. Wu, J. Zhang, B.B. He, H.W. Wang, R. Wang, Y.S. Gong, Appl. Catal. B **241**, 159 (2019). https://doi.org/10.1016/j.apcatb.2018.09.037
30. Y.Z. Zhang, S.C. Zong, C. Cheng et al., Appl. Catal. B **233**, 80 (2018). https://doi.org/10.1016/j.apcatb.2018.03.104
31. Y.M. Wang, H.Y. Cai, F.F. Qian et al., J. Colloid Interface Sci. **533**, 47 (2019). https://doi.org/10.1016/j.jcis.2018.08.039
32. B. Fei, Y.W. Tang, X.Y. Wang et al., Mater. Res. Bull. **102**, 209 (2018). https://doi.org/10.1016/j.materresbull.2018.02.041
33. J.J. Wu, N. Li, H.B. Fang, X. Li, Y.Z. Zheng, X. Tao, Chem. Eng. J. **358**, 20 (2019). https://doi.org/10.1016/j.cej.2018.09.208
34. P. Niu, L.C. Yin, Y.Q. Yang, G. Liu, H.M. Cheng, Adv. Mater. **26**, 8046 (2014). https://doi.org/10.1002/adma.201404057
35. S.E. Guo, Y.Q. Tang, Y. Xie et al., Appl. Catal. B **218**, 664 (2017). https://doi.org/10.1016/j.apcatb.2017.07.022
36. H.J. Yu, R. Shi, Y.X. Zhao et al., Adv. Mater. **29**, 8 (2017). https://doi.org/10.1002/adma.201605148
37. M. Wu, J.M. Yan, X.N. Tang, M. Zhao, Q. Jiang, ChemSusChem **7**, 2654 (2014). https://doi.org/10.1002/cssc.201402180
38. Y.O. Wang, M.K. Bayazit, S.J.A. Moniz et al., Energy Environ. Sci. **10**, 1643 (2017). https://doi.org/10.1039/c7ee01109a
39. Y. Hong, C. Li, D. Li et al., Nanoscale **9**, 14103 (2017). https://doi.org/10.1039/c7nr05155g
40. H. Li, H. Yu, X. Quan, S. Chen, Y. Zhang, ACS Appl. Mater. Interfaces. **8**, 2111 (2016). https://doi.org/10.1021/acsami.5b10613
41. N. Tian, Y.H. Zhang, X.W. Li et al., Nano Energy **38**, 72 (2017). https://doi.org/10.1016/j.nanoen.2017.05.038
42. F. Zeng, W.Q. Huang, J.H. Xiao et al., J. Phys. D **52**, 11 (2019). https://doi.org/10.1088/1361-6463/aae81a
43. J.Z. Chen, B. Li, J.F. Zheng et al., J. Phys. Chem. C **115**, 7104 (2011). https://doi.org/10.1021/jp2004369
44. P.X. Qiu, C.M. Xu, H. Chen et al., Appl. Catal. B **206**, 319 (2017). https://doi.org/10.1016/j.apcatb.2017.01.058
45. Q. Qiao, K. Yang, L.L. Ma et al., J. Phys. D **51**, 12 (2018). https://doi.org/10.1088/1361-6463/aac817